The Chilean Coastal Orographic Precipitation Experiment: Observing the Influence of Microphysical Rain Regimes on Coastal Orographic Precipitation

ADAM K. MASSMANN,[a,g] JUSTIN R. MINDER,[a] RENÉ D. GARREAUD,[b] DAVID E. KINGSMILL,[c] RAUL A. VALENZUELA,[c,d] ALDO MONTECINOS,[e] SARA LYNN FULTS,[f] AND JEFFERSON R. SNIDER[f]

[a] *Department of Atmospheric and Environmental Sciences, University at Albany, State University of New York, Albany, New York*
[b] *Department of Geophysics and Center for Climate and Resilience Research, Universidad de Chile, Santiago, Chile*
[c] *Cooperative Institute for Research in Environmental Sciences, University of Colorado Boulder, Boulder, Colorado*
[d] *Department of Atmospheric and Oceanic Sciences, University of Colorado Boulder, Boulder, Colorado*
[e] *Water Research Center for Agriculture and Mining, Universidad de Concepción, Concepción, Chile*
[f] *Department of Atmospheric Science, University of Wyoming, Laramie, Wyoming*

(Manuscript received 6 January 2017, in final form 19 June 2017)

ABSTRACT

The Chilean Coastal Orographic Precipitation Experiment (CCOPE) was conducted during the austral winter of 2015 (May–August) in the Nahuelbuta Mountains (peak elevation 1.3 km MSL) of southern Chile (38°S). CCOPE used soundings, two profiling Micro Rain Radars, a Parsivel disdrometer, and a rain gauge network to characterize warm and ice-initiated rain regimes and explore their consequences for orographic precipitation. Thirty-three percent of foothill rainfall fell during warm rain periods, while 50% of rainfall fell during ice-initiated periods. Warm rain drop size distributions were characterized by many more and relatively smaller drops than ice-initiated drop size distributions. Both the portion and properties of warm and ice-initiated rainfall compare favorably with observations of coastal mountain rainfall at a similar latitude in California. Orographic enhancement is consistently strong for rain of both types, suggesting that seeding from ice aloft is not a requisite for large orographic enhancement. While the data suggest that orographic enhancement may be greater during warm rain regimes, the difference in orographic enhancement between regimes is not significant. Sounding launches indicate that differences in orographic enhancement are not easily explainable by differences in low-level moisture flux or nondimensional mountain height between the regimes.

1. Introduction and background

In the midlatitudes, coastal mountain ranges of moderate height (500–1500 m) and width (10–100 km) can increase precipitation up to 6 times that of the upwind ocean and downwind land (e.g., Douglas and Glasspoole 1947; Bergeron 1949; Browning et al. 1974; Hill et al. 1981; Neiman et al. 2002; Reuder et al. 2007; Minder et al. 2008; Garreaud et al. 2016). Such strong orographic precipitation enhancement requires that 1) flow passes over terrain, 2) incoming flow be at or near saturation, and 3) water condensed in flow lifted by the terrain reaches the ground prior to evaporating in descent leeward of the mountains. For a flow satisfying these three requirements, orographic enhancement of precipitation will generally increase with increasing cross-barrier moisture flux (e.g., Smith and Barstad 2004; Neiman et al. 2002).

The presence of the first requirement is often assessed using the nondimensional mountain height parameter NH/U, where N is the static stability of the flow, H is the barrier height, and U is the cross-barrier wind speed. Theoretically, when NH/U is less than some mountain geometry-dependent threshold (generally about 1) flow passes over mountains, but when NH/U is greater than this threshold flow may become blocked and reverse or split to pass around a barrier (e.g., Smith 1980; Baines and Smith 1993). Midlatitude cyclones impacting modest barriers along west coasts of continents often provide low NH/U and flow at or near saturation, which additionally satisfies the second requirement. In particular, warm-sector "atmospheric rivers" (Zhu and Newell 1998) found in many of these cyclones provide, by definition, large integrated moisture fluxes and ideal conditions for significant orographic enhancement (Ralph et al. 2006).

[g] Current affiliation: Department of Earth and Environmental Engineering, Columbia University, New York, New York

Corresponding author: Adam K. Massmann, akm2203@columbia.edu

DOI: 10.1175/JHM-D-17-0005.1

Unlike the first two requirements, which depend almost exclusively on large-scale atmospheric conditions, the third requirement depends on much smaller-scale atmospheric processes. Defining relevant time scales allows one to conceptualize the necessary ingredients for condensed water to reach the surface in an orographic flow, and this approach has been used to represent microphysical processes in the linear theory numerical model of Smith and Barstad (2004) (hereafter LT-model). In the LT-model, condensate produced by mountain-wave-induced ascent is subjected to two time delays before reaching the ground as precipitation: a delay for condensate to grow and form into hydrometeors (τ_c), and a delay for precipitation to fall to the surface (τ_f). The introduction of an additional advective time scale representing the amount of time it takes for flow to traverse the terrain and experience leeward descent on the scale of a mountain range τ_{adv} allows one to define the ingredients necessary for the third requirement. For significant orographic enhancement, τ_{adv} must be much larger than the sum of τ_c and τ_f (Jiang and Smith 2003). Narrow coastal mountain ranges (10–100 km) have relatively smaller τ_{adv} than broader mountain ranges for a given cross-barrier flow speed, so microphysical time scales (τ_c and τ_f) more likely constrain orographic precipitation efficiency for such ranges. In addition to moisture and condensate source, which may be determined by synoptic-scale conditions, microphysical and cloud-scale dynamical processes play key roles in determining τ_c and τ_f (Cannon et al. 2012; Miltenberger et al. 2015). Specific microphysical mechanisms that may enable efficient precipitation production (small τ_c and τ_f) and strong orographic enhancement over narrow mountain ranges are the "seeder–feeder" processes and rapid warm rain autoconversion.

The seeder–feeder mechanism induces rapid conversion of cloud water to hydrometeors (small τ_c) and increased hydrometeor size (small τ_f), which allow for orographic enhancement over narrow barriers (e.g., Bergeron 1965; Carruthers and Choularton 1983). In this process, "seed" precipitation originating as ice aloft sweeps out large amounts of cloud water in shallow orographic "feeder" clouds through collection. Studies in the coastal hills of the British Isles (e.g., Bader and Roach 1977; Hill et al. 1981), the Olympic Mountains of North America (e.g., Minder et al. 2008), and the California Coast Range (e.g., White et al. 2003) have identified the seeder–feeder process as integral to orographic precipitation. Research in the California Coast Range used melting-level detection from profiling radars to identify periods when the seeder–feeder mechanism may be present (e.g., White et al. 2003; Martner et al. 2008; White et al. 2015). We call these periods ice-initiated rain, which is synonymous with the "brightband" rain term used in previous research (e.g., White et al. 2003; Martner et al. 2008; White et al. 2015). Given an ice-initiated rain designation, seeder–feeder processes are active if a low-level orographic cloud is present, which is usually the case in coastal mountain ranges with moist onshore flow (e.g., Kingsmill et al. 2016). Within these low-level orographic clouds "warm rain" microphysical processes, such as collision–coalescence between drops initiated at temperatures greater than 0°C, are also active and interact with ice-initiated seeds.

In cases without seeding from ice aloft, low-level enhancement over narrow barriers may also be accomplished exclusively by these "warm rain" processes in shallow orographic clouds if efficient autoconversion of cloud water to rain occurs via collision–coalescence (e.g., Blanchard 1953; White et al. 2003; Smith et al. 2012). Recent observations in the California Coast Range suggest that warm orographic rain clouds are capable of producing sufficiently small τ_c and τ_f relative to τ_{adv} to induce substantial orographic precipitation (e.g., White et al. 2003, 2015; Neiman et al. 2005, 2016; Coplen et al. 2015; Kingsmill et al. 2016). Such orographic warm rain clouds are typically associated with strong, moist upslope flow (White et al. 2003; Neiman et al. 2005; Kingsmill et al. 2016) and precipitation drop size distributions (DSDs) that contain copious small drops (Blanchard 1953; Martner et al. 2008). Either giant sea salt CCN or the general cleanliness of maritime air (fewer CCN leads to larger drops for given amount of cloud water) could facilitate growth of cloud water into larger droplets with greater fall speeds (relative to continental air). This would offer an explanation for microphysical efficiency in coastal warm rain clouds (e.g., Johnson 1982; Szumowski et al. 1999; Jensen and Nugent 2017).

While coastal California studies successfully identified warm rain processes as important contributors to coastal orographic precipitation, their conclusions were limited by a spatially sparse rain gauge network. Additionally, research on warm and ice-initiated regimes has largely focused on this one geographic location, although active research projects are exploring warm rain and ice processes in the Olympic Mountains (e.g., Zagrodnik et al. 2016; Houze et al. 2017). Through observations from a field campaign in the Southern Hemisphere, this study seeks to test the generalization of conclusions reached in California to other parts of the globe, while improving understanding on the relationships among rain regime, upwind flow, and orographic precipitation enhancement.

a. The Nahuelbuta Mountains

The Nahuelbuta Mountains of south-central Chile, located around 37.6°S on the Pacific coast (Fig. 1),

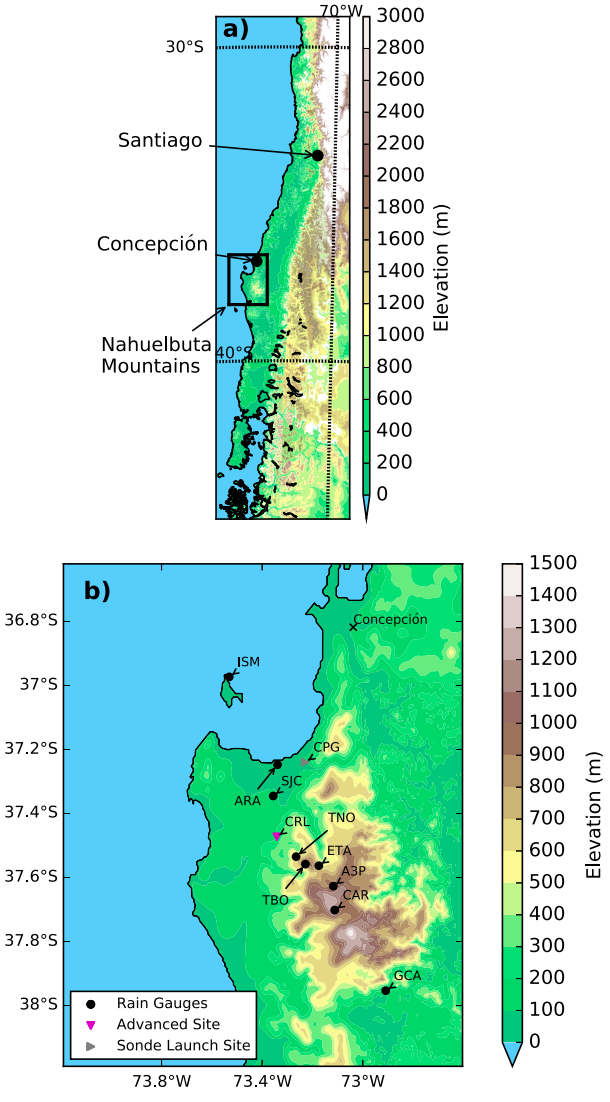

FIG. 1. The field study region: (a) location within Chile (depicted by the black box) and (b) detailed map of the Nahuelbuta Mountains and study sites. Rain gauge locations are: ISM, ARA, SJC, TNO, TBO, ETA, A3P, CAR, and GCA. An advanced study site is located at CRL with additional radar, disdrometer, and surface meteorological measurements. The radiosonde launch site is at CPG. The city of Concepción is shown for reference.

are a heavily forested semielliptical massif about 150 km long and 100 km wide. The highest point reaches above 1500 m MSL, and there is an extensive area between 1000 and 1200 m MSL. To the east of the Nahuelbuta is a broad central valley that separates them from the Andes Mountains that rise to about 2 km at this latitude.

The region's position between the mean Southern Hemisphere storm track to the south and the South Pacific high create a temperate Mediterranean climate (Köppen climate classification Csb; Peel et al. 2007). Precipitation is mostly generated by midtropospheric troughs and surface depressions (Falvey and Garreaud 2007; Viale and Nuñez 2011; Garreaud 2013; Garreaud et al. 2016). At a nearby climate station (Concepción, Chile), 70% of precipitation falls during austral winter (May–August) from 1970 to 2000 (Fontannaz 2001). Snowfall is minimal and limited to the highest elevations of the Nahuelbuta.

The recent Andean Frontal Experiment (AFEX; Garreaud et al. 2016) examined rainfall over the Nahuelbuta using 2 years of data collected with a dense network of 15 data-logging tipping-bucket rain gauges. Most of the gauges were deployed along a northwest–southeast-oriented transect to capture along-wind variations in precipitation associated with the typical northwesterly flow during major rainfall events in the region. AFEX observations reveal a dramatic orographic enhancement: wintertime rainfall increases from around 1000 mm offshore to nearly 4000 mm in the central Nahuelbuta Mountains about 50 km away.

On monthly to annual time scales, the spatial pattern of precipitation over the Nahuelbuta was well represented by a high-resolution forecast model (WRF, run with a 1-km horizontal grid) and the LT-model [Garreaud et al. (2016); see their Fig. 8]. However, the LT-model was unable to represent transient rainbands and very local precipitation maxima that were resolved by WRF. These rainbands strongly influence precipitation patterns at the time scale of individual storms and shorter. Although the source of transient rain patterns includes terrain-induced nonlinearities in the flow (e.g., blocking), convection, and temporal and spatial variability in the synoptic rain pattern (none of which are represented in the LT-model), WRF simulations suggested that the primary sources of precipitation variability in the Nahuelbuta were a combination of linear orographic effects and synoptic-scale variability (Garreaud et al. 2016).

Garreaud et al. (2016) explored the interplay between synoptic events and orographic enhancement by examining 25 frontal passages during the austral winter of 2011. Orographic enhancement as quantified by "orographic difference," or the difference in accumulation between mountain and upwind sites, was relatively consistent both between and during storms. However, relative orographic enhancement quantified by the "orographic ratio," or the ratio of mountain to upwind precipitation, was reduced as background synoptic precipitation increased during frontal passages. One might expect these metrics of orographic enhancement to depend on variations in microphysical regime (such as warm rain versus seeder–feeder) given the narrow width of the Nahuelbuta, but Garreaud et al. (2016) lacked the instrumentation required for such an analysis.

b. Overview

The Chilean Coastal Orographic Precipitation Experiment (CCOPE) builds upon Garreaud et al. (2016) by reexamining orographic enhancement in the Nahuelbuta within a framework of warm and ice-initiated rain regimes. Contrasting rainfall observations between these regimes will quantify the consequences of varying microphysical processes for orographic precipitation, specifically testing if and how seeding from ice aloft matters for orographic enhancement. Additionally, the Nahuelbuta's geographic similarities to the California Coast Range will allow direct comparison with previous studies. The California–Nahuelbuta comparison may also provide indirect evidence for the importance of CCN concentration for orographic precipitation processes because incoming flow from the southern Pacific Ocean is expected to have relatively less aerosol content (e.g., Hamilton et al. 2014) and fewer cloud droplets in boundary layer clouds (Bennartz 2007) than its northern Pacific counterpart. However, aerosol concentrations at a given location in either hemisphere may deviate from these bulk patterns depending on local conditions.

Section 2 describes the instrumentation, data, and methods used in this analysis. A case study of a representative precipitation event is presented in section 3. Section 4 examines campaign-length surface rainfall characteristics as a function of rain regime, and section 5 tests the generality of California orographic precipitation research through comparisons to CCOPE observations. Finally, section 6 presents conclusions and a summary.

2. Instrumentation and data

CCOPE deployed instrumentation to characterize cross-barrier precipitation patterns, upwind thermodynamic profiles, size and number concentration of surface precipitation, and the vertical structure of precipitation. Aerosol measurements were also collected at a coastal site, but these are not discussed in this study. With some exceptions the CCOPE instrumentation described in the following sections was operational from 22 May 2015 to 14 August 2015. All the below-described data are archived and available online (at https://www.eol.ucar.edu/field_projects/CCOPE-2015).

a. Rain gauge network

Eight Onset HOBO RG3-M tipping-bucket rain gauges were deployed in a northwest–southeast transect across the Nahuelbuta (Fig. 1). The rain gauges measured precipitation with a 0.2 mm per tip resolution. Additionally, rain gauges with a 0.1 mm per tip resolution were deployed at Arauco (ARA) and Curanilahue (CRL). Most gauge locations were identical to those used during AFEX: San Jose de Colico (SJC), CRL, Torre Norte (TNO), Torre Bomberos (TBO), Escuela Trongol Alto (ETA), Alto Tres Pinos (A3P), and Cerro Alto Arauco (CAR). Guadaba Central (GCA) and Isla Santa María (ISM) were deployed in similar locations to AFEX sites Torre El Sauce (TES) and ISM.

Rain gauges were generally located a horizontal distance away from surrounding obstacles equal to at least 4 times the height of the obstacle. Practical constraints resulted in some sites being located in clearings with few upwind obstructions under prevailing winds (ISM, TBO, TNO, A3P). High winds at these sites could be a source of nonnegligible gauge undercatch (e.g., Sieck et al. 2007), which could be exacerbated during rain dominated by small drops (Nešpor and Sevruk 1999).

Data availability varied for each location. CRL and ARA were available for the entire campaign period. TBO, ETA, CAR, and GCA were available for the entire field campaign with the exception of a period from 11 to 26 June. ISM, SJC, TNO, and A3P all had additional periods of downtime. Storm-scale analysis (section 3) will use all operational rain gauges. Campaign-length rain gauge analysis (section 4) will utilize ARA, CRL, TBO, ETA, CAR, and GCA, as this collection of gauges strikes a good balance between temporal and spatial sampling. Table 1 provides a summary of site names, locations, data availability, and AFEX equivalents.

b. Measurements at Curanilahue

CRL sits in a developed valley (137 m MSL) at the transition from foothills to the high peaks of the Nahuelbuta (Fig. 1). At this site the vertical structure of precipitation, the size distribution of surface rainfall, basic surface meteorology, and precipitation accumulation were measured.

An OTT Parsivel disdrometer was located at CRL. This laser-based optical instrument counts precipitation size and fall speed in 32×32 bins at a 2-min temporal resolution. The two smallest size bins are outside the measurement range of the instrument and are not used (OTT 2009). Additionally, we remove the third-smallest size bin (diameter < 0.37 mm) because the Parsivel systematically undercounts raindrops in those bins based on side-by-side comparisons with the Joss–Waldvogel disdrometer (Joss and Waldvogel 1967) at various locations in the United States (S. E. Yuter 2015, personal communication). The Joss–Waldvogel disdrometer is more sensitive to smaller drops than the Parsivel, and the discrepancy between the two instruments casts doubt on the Parsivel's ability to measure drops of that size. Two-minute estimates of mean volume diameter D_m, which is

TABLE 1. Name, location, elevation, and data availability of rain gauges used in CCOPE. AFEX equivalent rain gauge locations are also noted where relevant, with an asterisk denoting locations that are similar (i.e., within 5 km) but not identical to AFEX locations. "Start" refers to the campaign start date of 22 May 2015, and "End" refers to the campaign end date of 14 Aug 2015.

Rain gauge	Abbreviation	AFEX equivalent	Latitude	Longitude	Elevation (m)	Missing data period
Isla Santa Maria	ISM	ISM*	−36.9756	−73.5287	61	Start–22 Jun 2015
Arauco	ARA	N/A	−37.2499	−73.3393	58	—
San Jose de Colico	SJC	ECO	−37.3478	−73.3564	153	Start–24 Jun 2015
Curanilahue	CRL	CUR	−37.4753	−73.3423	137	—
Torre Norte	TNO	TNO	−37.5374	−73.2663	734	11 Jun 2015–End
Torre Bomberos	TBO	TBO	−37.5606	−73.2293	996	11–26 Jun 2015
Escuela Trongol Alto	ETA	ETA	−37.5655	−73.1764	752	11–26 Jun 2015
Alto Tres Pinos	A3P	A3P	−37.6293	−73.1192	1045	Start–26 Jun 2015
Cerro Alto Arauco	CAR	CAR	−37.7041	−73.1136	1384	11–26 Jun 2015
Guadaba Central	GCA	TES*	−37.9553	−72.9102	131	—

the ratio of the fourth to the third moments of the drop size distribution; $\log_{10}$ of rain rate; liquid water content (LWC); radar reflectivity factor; and total volumetric number concentration N_d (particles per m^3) are calculated from Parsivel DSDs [derived following Yuter et al. (2006)]. These quantities are also calculated for half-hour intervals during periods in which greater than 0.5 mm of precipitation fell for better comparison to Martner et al.'s (2008) California study. The half-hourly data are used in the analysis in section 4, while the 2-min resolution data are used in the time series in section 3. One limitation of the Parsivel disdrometer is its inability to measure very small drops. Given that warm rain regimes are characterized by, on average, smaller drop size (Martner et al. 2008), one might expect drop-size-derived quantities to be more biased during warm rain periods than ice-initiated periods due to the large increase in drops of small size during warm rain periods. This bias will be further discussed in section 4a.

Two 24-GHz Metek Micro Rain Radars (MRRs) were collocated at CRL and provided vertical profiles of reflectivity, Doppler velocity, and spectral width at 1-min temporal resolution. The instruments have 32 range gates with fixed range resolution, but data from the bottom three and the topmost range gates are removed following Maahn and Kollias (2012). The first range gate is not usable (it corresponds to 0 m height), while the next two range gates are biased by near-field effects and the topmost range gate is very noisy. One radar was set to a fine range resolution to sample near-surface precipitation characteristics with range gates centered every 50 m between 150 and 1550 m above the surface. The second radar was set to sample deep in the atmosphere with range gates centered every 200 m between 600 to 6200 m above the surface.

Before analysis of MRR data, we applied Maahn and Kollias's (2012) postprocessing to increase the effective sensitivity of the radar, better interpret upward Doppler velocities, and remove noise and artifacts from the data. Maahn and Kollias's (2012) algorithm is used because it gives specific attention to Doppler velocity profiles integral to CCOPE analysis. This contrasts with other improvement techniques that focus on DSD profiles or reflectivity (e.g., Peters et al. 2005; Adirosi et al. 2016).

Maahn and Kollias's (2012) algorithms were developed primarily for observations of snow with a low signal-to-noise ratio. Their suitability for use with observations of moderate-to-heavy rain and the melting level is uncertain. This uncertainty is compounded by the radar's K-band wavelength, which attenuates substantially at high rain rates. At moderate rain rates of $2\ mm\ h^{-1}$ one-way attenuation due to rain is about $0.2\ dB\ km^{-1}$, but at rain rates of $50\ mm\ h^{-1}$ this increases to about $10\ dB\ km^{-1}$ (Fabry 2015).

To test the MRR's suitability for measuring orographic rain, we compared MRR observations to a more sensitive radar at a nonattenuating frequency in the California Coast Range (see appendix A). Based on this comparison we concluded that MRR reflectivity profiles should only be used for qualitative analysis of coastal orographic rainfall because of biases likely associated with attenuation. However, we do use MRR Doppler velocity data to detect melting layer signatures and discriminate between ice-initiated and warm rain regimes, following a similar methodology as White et al. (2003). Appendix B describes our methodology and the accuracy of the method.

c. *Derivation of ice-initiated and warm rain time series*

To distinguish between rainfall regimes, we applied an ice-initiated versus warm rain classification as described in appendix B. To summarize the classification technique, we use MRR-observed gradients of Doppler velocity to identify precipitation melting levels synonymous with ice-initiated periods. One departure from the

technique described in appendix B is that we leveraged the increased tip resolution of CCOPE rain gauges (relative to the rain gauge used in appendix B) and applied the algorithm to all half-hour periods in which 0.2 mm or more of precipitation fell at CRL. Prior to regime classification, extended ''convective'' periods were subjectively removed for all rain gauges when MRR profiles at CRL exhibited high variability. To avoid subjectively biasing results, no attempt is made to remove short-duration convective periods observed within both warm and ice-initiated rain regimes. As a result ''convective'' periods are longer-duration events of intermittent convection at least a day in length. These periods account for a relatively small portion (16%) of the total observed rainfall at CRL during the field campaign, which is consistent with AFEX WRF analysis, suggesting that convection is not a major contributor to precipitation.

The rain regime classification was applied to all rain gauge sites using data from CRL. We assume that ice-initiated (warm) periods are predominantly associated with the presence (absence) of midlevel synoptically forced ascent so that variations in rainfall regime are associated with variations in midlevel synoptic-scale forcing. Since horizontal scales of synoptic variability [O(100–1000) km] will generally be much larger than the horizontal scale of the gauge network [O(10) km], projecting rain regime identification at CRL across the gauge network should be a reasonable approach. While frontal passages with shorter horizontal variability may violate these assumptions, given no systematic bias for warm rain or ice-initiated rain occurrence within frontal evolution, one might expect errors in regime identification to balance out over a long time series. Nevertheless, there are still uncertainties as to how conditions at CRL generalize to other rain gauges, which are manifested by a nonnegligible third type of rainfall: ''unclassified rain.'' Unclassified rain falls at a site while CRL receives less than 0.2 mm of precipitation in a half-hour and no MRR rain regime classification is made.

d. Radiosondes and IOPs

To obtain upwind profiles of the atmosphere, InterMet iMet-1 balloon radiosondes were launched during intensive observation periods (IOPs) from about 30 km north of CRL at Carampangue (CPG). These IOPs targeted periods of sustained rainfall associated with frontal passages. In total 26 radiosondes were launched during six IOPs. Within each IOP, launches were timed to sample diverse storm sectors and rain regimes. We focus on the characteristics of the low-level flow, since it is expected to exert strong control on orographic enhancement over the Nahuelbuta. For a 500–2000-m layer we calculate integrated water vapor (IWV), IWV flux, mean wind speed and direction, and N_mH/U. The moist version of the Brunt–Väisälä frequency N_m (Durran and Klemp 1982) is used in place of the dry version of N in N_mH/U because flow is generally at or near saturation during the precipitation events targeted for IOPs. Soundings launched from CPG sampled the upwind, unperturbed environment before they reached 2000 m. Additionally, some soundings terminated early, so using a deeper layer above 2000 m would decrease sample size. Measurements below 500 m are more likely to be influenced by local surface heterogeneities and so are not used. For calculating N_mH/U, a height of 1250 m is used for H (as in Garreaud et al. 2016), and U and N_m are density-weighted means for the layer. Frequency N_m is calculated following Eq. (36) in Durran and Klemp (1982), and imaginary N_m are treated as zero for the mean calculation.

3. Case study of contrasting rainfall regimes

The following case study from 2200 UTC 7 July to 2000 UTC 8 July 2015 provides detailed observations of representative periods of ice-initiated and warm rain within a storm characterized by significant precipitation and orographic enhancement. The event was selected because it had two well-defined, long-duration periods of warm and ice-initiated rain, each with a well-timed sounding launch that provides a representative thermodynamic profile. Additionally, all CCOPE instrumentation was fully functional for the duration of the event.

a. Synoptic evolution

Figures 2 and 3 track the evolution of the synoptic storm using GOES satellite imagery and GFS model analysis, respectively. At 0300 UTC 8 July 2015 thermal infrared imagery shows widespread high cloud tops (Fig. 2a) and elevated upper-level water vapor (Fig. 2c) over south-central Chile associated with synoptic forcing for midtropospheric lift (Fig. 3a). By 1500 UTC 8 July the high cloud tops have vacated the region and intrusion of dry upper-level air has begun, while low-level clouds are still present (Figs. 2b,d). This upper-level drying is associated with a decrease in midtropospheric vertical motion (Fig. 3b). High IWV and cross-barrier 850-hPa flow provide strong forcing for orographic precipitation at both times (Figs. 3c,d). Given that the cold front is rather weak (as per the low-level temperature contrast) and the low-level winds impinging the Nahuelbuta changed their direction only slightly as the storm evolved, this event may be a closer analog to the warm storms examined in Garreaud (2013)

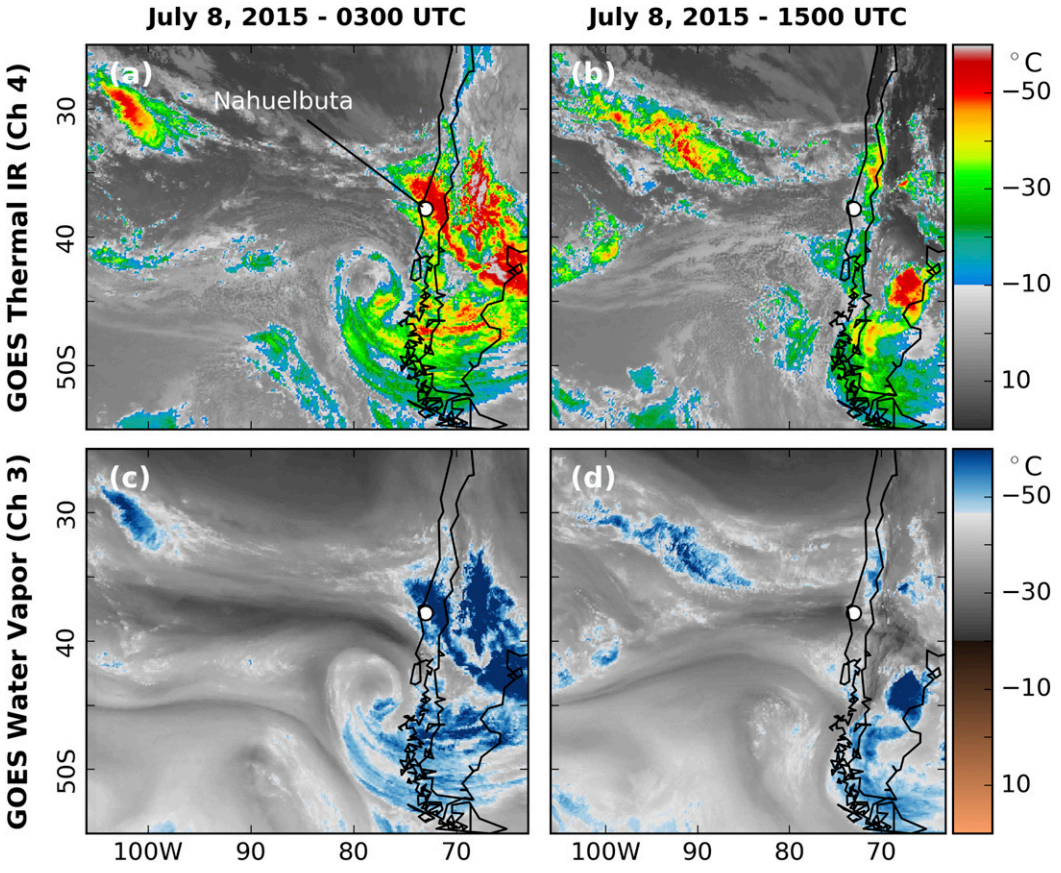

FIG. 2. Geostationary satellite imagery for the 8 Jul 2015 case study. (top) Thermal infrared imagery (GOES-IR4) from (a) 0300 UTC and (b) 1500 UTC 8 Jul. (bottom) Water vapor imagery (GOES-IR3) from (c) 0300 UTC and (d) 1500 UTC 8 Jul.

than the more marked frontal passages examined during AFEX (Garreaud et al. 2016).

b. *Time series and soundings*

Figure 4 provides a time series of CCOPE data for the event. An extended period of mostly ice-initiated rain coincides with the synoptic forcing seen at the beginning of the event in section 3a (0000–0400 UTC). Ice aloft suggests mid- to upper-level forcing for ascent, which is observed in this specific case study (Fig. 3). The ice-initiated rain and presence of a melting level is evident from the large gradient in Doppler vertical velocity at about 2.5 km corresponding to the melting layer. During this period MRR echoes reach elevations of 4000–6000 m. Parsivel data show a broad DSD including a substantial number of drops with diameters up to and exceeding 2 mm. Accumulations in the mountains (ETA) and foothills (CRL) are nearly identical, while the coast (ARA) accumulates about half has much precipitation.

A sounding at 0229 UTC (Fig. 5a) shows humid air aloft, with conditions at or near saturation with respect to water, up to the termination of the sounding at 400 hPa. The large low-level (500–2000 m) IWV flux ($231.4\,\mathrm{mm\,m^{-1}\,s^{-1}}$), wind direction (322°), and low N_mH/U (0.52) provide the necessary ingredients for significant orographic precipitation on the northwest slopes of the Nahuelbuta. An elevated layer of instability at 800 hPa may support some weak embedded convection. The winds turn counterclockwise with height, particularly through an inversion at 650 hPa, suggesting warm air advection (WAA) in the layer and synoptic-scale forcing for vertical motion.

The atmospheric moisture profile, Parsivel data, and radar data present a coherent image of ice-initiated rain during this period of the storm: saturation aloft initiates and grows ice crystals which fall through any present orographic clouds. These ice-initiated drops interact with and sweep out cloud water, including warm rain drops (i.e., drops initiated at temperatures above 0°C). This produces the observed broad DSD. Despite the flow's conduciveness for windward orographic enhancement, there was relatively little enhancement between the

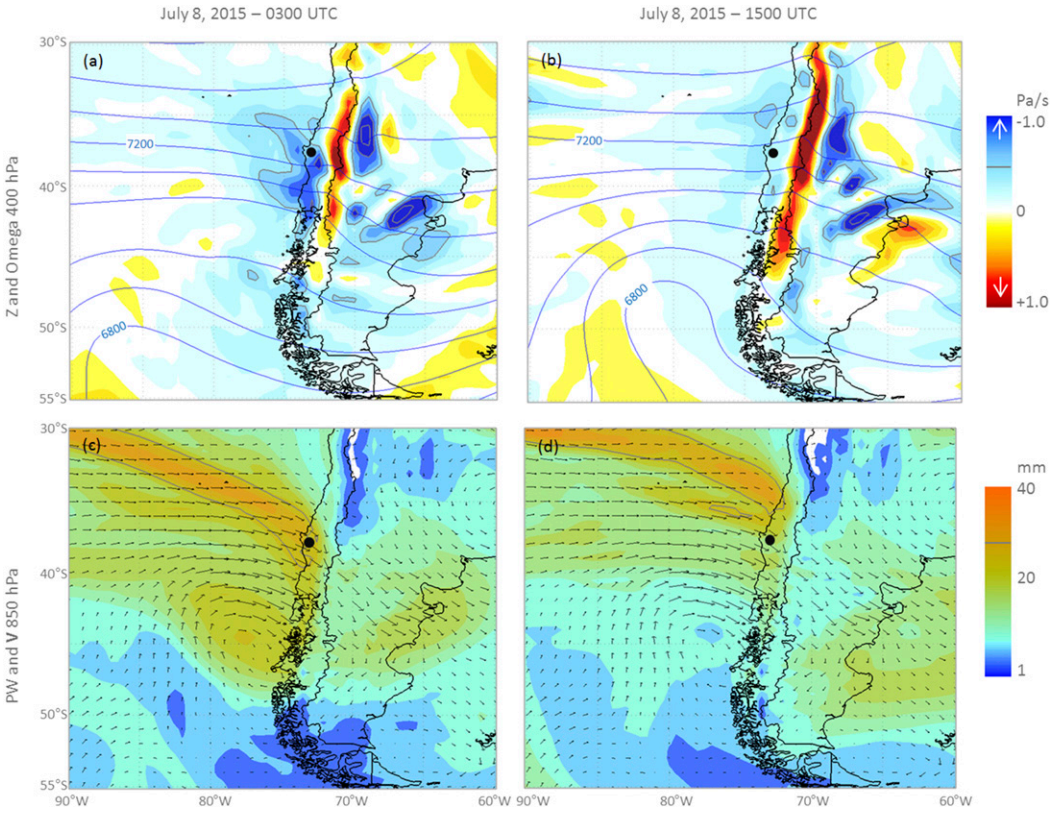

FIG. 3. Synoptic circulation features for the 8 Jul 2015 case study. Pressure vertical velocity (omega; colors) and geopotential height (contoured in blue, every 80 gpm) at the 400-hPa level for (a) 0300 UTC and (b) 1500 UTC 8 Jul. The gray contours outline areas with omega $< -0.5\,\mathrm{Pa\,s^{-1}}$. Total precipitable water (PW; in colors; gray contours outline areas with PW > 28 mm) and 850 hPa winds for (c) 0300 UTC and (d) 1500 UTC 8 Jul. The fields are a 3-h GFS forecasts initialized at 0000 and 1200 UTC 8 Jul, respectively. The small black circle indicates the location of the Nahuelbuta in the southern coast of Chile.

foothills and nearby mountain gauges, but windward enhancement was apparent between the coastal site (ARA) and the foothills and mountains (CRL, ETA).

The rainfall transitions from ice-initiated to warm rain between 0400 and 0600 UTC 8 July. After the transition there is an extended period of mostly warm rain for the remainder of the event. During this period accumulation tapers off at the coast, while the mountain sites continue to accumulate precipitation at a rate comparable to the ice-initiated period. MRR echoes seldom exceed 2000 m.

A sounding launched at 1027 UTC (Fig. 5b) from CPG shows dry air above 600 hPa, consistent with the water vapor imagery (Fig. 2d). Additionally, directional wind shear is primarily constrained to the planetary boundary layer with the exception of some turning between 950 and 850 hPa, which may indicate low-level WAA. The elevated instability in Fig. 5a is mostly gone in Fig. 5b. The sounding still retains most of the features conducive to orographic enhancement observed in the ice-initiated sounding: large low-level (500–2000 m) IWV flux ($204.4\,\mathrm{mm\,m^{-1}\,s^{-1}}$), wind direction (298°), and low N_mH/U (0.55). The DSD during warm rain periods has fewer large drops, but many small drops. The warm rain period is punctuated by intermittent periods of deep precipitation, particularly at around 1200 and 1600 UTC. At these times, clear spikes in the peak drop size in the DSD coincide with deeper radar returns extending above the melting level. Given the short time scale of this variability, we consider these times to be a signal of convection; however, very localized stratiform rainbands would exhibit a similar pattern (e.g., Hobbs 1978). The automated classification struggles with these times, classifying some as warm and some as ice initiated. In particular, a significant portion of ARA's accumulation occurs during a period of deep precipitation that is objectively, yet likely erroneously, identified as warm rain.

With the exception of these brief anomalous periods, the data present a similarly clear picture of warm rain: shallow rainfall produced by orographic clouds via collision–coalescence that do not rely on ice falling from aloft to transport cloud water to the surface. While synoptic conditions provide the high low-level IWV flux

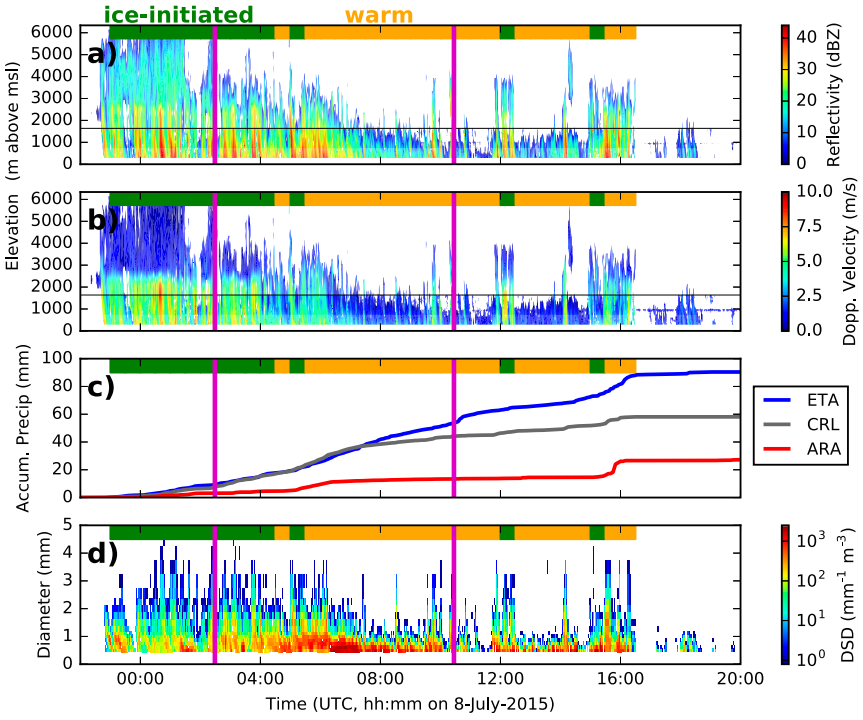

FIG. 4. Time series of CCOPE data from the case study: (a) MRR reflectivity; (b) MRR Doppler velocity (positive is toward radar); (c) rainfall accumulation at ARA, CRL, and ETA; and (d) Parsivel DSD. Objectively derived ice-initiated rain periods are marked by green bars at the top of each panel, and warm rain periods are indicated in orange. Magenta vertical bars indicate two sounding launches from CPG, which are plotted in Fig. 5. Additionally, the horizontal black line in (a) and (b) indicates the boundary between data sourced from the fine (50 m) resolution MRR (elevation 287–1687m) and the coarse (200 m) resolution MRR (elevation 1687–6337 m).

and moderate stability necessary for significant orographic precipitation, the lack of moisture aloft implies that synoptic forcing for lift is secondary in generating precipitation. During warm rain periods (e.g., 0600–1200 UTC, Fig. 5c) the general absence of precipitation at ARA and the increase in accumulation rate between the mountains and foothills suggests a rain regime for which orography has a dominant influence on the spatial precipitation distribution.

c. *Bulk observations of rain patterns*

Figure 6 shows the pattern of rainfall across the gauge network for the entire event, as well as precipitation totals during warm and ice-initiated periods. The total rainfall for the event (Fig. 6a) exhibits strong orographic enhancement. Precipitation increases through the upwind and windward gauges from 10 mm at ISM to about 90 mm at ETA. CAR has comparable precipitation to ETA while precipitation tapers off rapidly in the lee, to about 20 mm at GCA.

Figure 6b presents the cross-barrier pattern of precipitation during ice-initiated periods. Rainfall is relatively spatially homogeneous across the mountain and foothill sites, with much less precipitation falling at ISM, ARA, and GCA. Potential explanations for homogeneity in the foothills and mountains include upstream tilting of mountain waves or partial blocking of the flow, either of which could lead to orographic ascent and rainfall enhancement upwind of the windward slopes (e.g., Hughes et al. 2009; Valenzuela and Kingsmill 2015).

Warm rain accumulations are shown in Fig. 6c. Rainfall accumulations increase from ISM, through the foothills, and up to the windward peaks at TBO and ETA. The high sites (TBO, ETA, and CAR) have similar precipitation amounts, with the exception of A3P. The discrepancy in accumulation between A3P and nearby gauge locations ETA and CAR suggests that A3P suffered measurement error during the event. Overall, accumulated precipitation was greater during warm rain periods than ice-initiated periods for this event, in part because warm rain periods were longer in total duration (10.5 h) than ice-initiated periods (7 h). For example, at CRL rain rates were similar between

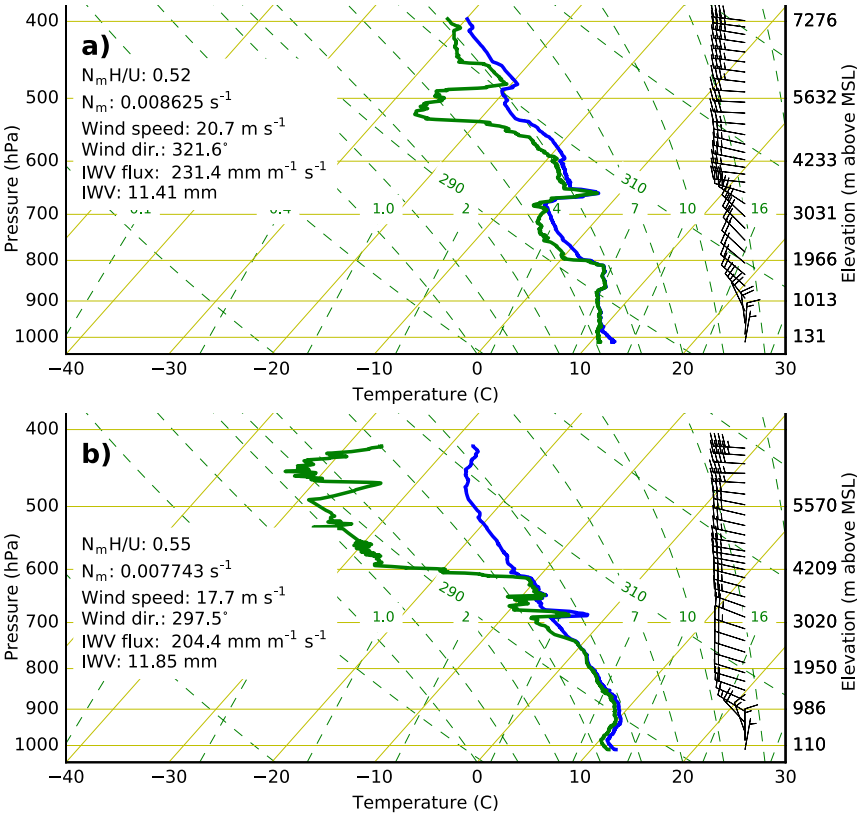

FIG. 5. Skew T–log$p$ plots of soundings launched from CPG during the (a) ice-initiated period (0229 UTC 8 Jul 2015) and (b) warm rain period (1027 UTC 8 Jul 2015) of the case study. Mean sounding metrics relevant for orographic precipitation are printed for a layer from 500 to 2000 m. These are N_mH/U, N_m, mean wind speed, mean wind direction, IWV flux, and IWV. Because of software constraints, wind barbs are plotted using Northern Hemisphere conventions (barbs above for westerlies) rather than Southern Hemisphere conventions (barbs below for westerlies).

warm (3.34 mm h^{-1}) and ice-initiated (3.64 mm h^{-1}) periods, while in the mountains rain rates were greater during warm rain periods (5.90 mm h^{-1} at ETA) relative to ice-initiated periods (3.71 mm h^{-1} at ETA).

Both rain regimes exhibit strong orographic enhancement despite substantial differences in midtropospheric humidity, echo depth, microphysical process, and DSDs observed. During warm rain periods, enhancement is strong despite the lack of seeding aloft and the short advection time scale over which collision–coalescence has to act. The enhancement appears more closely tied to the topography than during ice-initiated periods. Whether this signal is significant and observed throughout the field campaign will be addressed in section 4.

4. Campaign-length observations in the Nahuelbuta Mountains

We now examine campaign-length surface rainfall characteristics in the Nahuelbuta Mountains. In total 955.1 mm of precipitation fell at CRL from 22 May to 14 August. Of this, 33% (311.5 mm) fell during warm rain periods, 50% (476.9 mm) fell during ice-initiated periods, 16% (156.4 mm) fell during subjectively determined convective periods, and 1% (10.3 mm) fell during unclassified rain periods. The total duration of warm rain periods was 153 h, and the total duration of ice-initiated periods was 145 h.

a. *Comparison of DSD-derived rainfall quantities between warm and ice-initiated periods*

Figure 7 shows frequency distributions of the DSD-derived quantities at CRL for both warm and ice-initiated periods. Differences between warm and ice-initiated DSDs seen in Fig. 4 are consistent and apparent in these campaign-length derived quantities. Figures 7a and 7b show that warm rain is characterized by numerous small drops while ice-initiated rain is characterized by fewer drops but a broader DSD that includes larger drops. The frequency distribution of LWC is similar

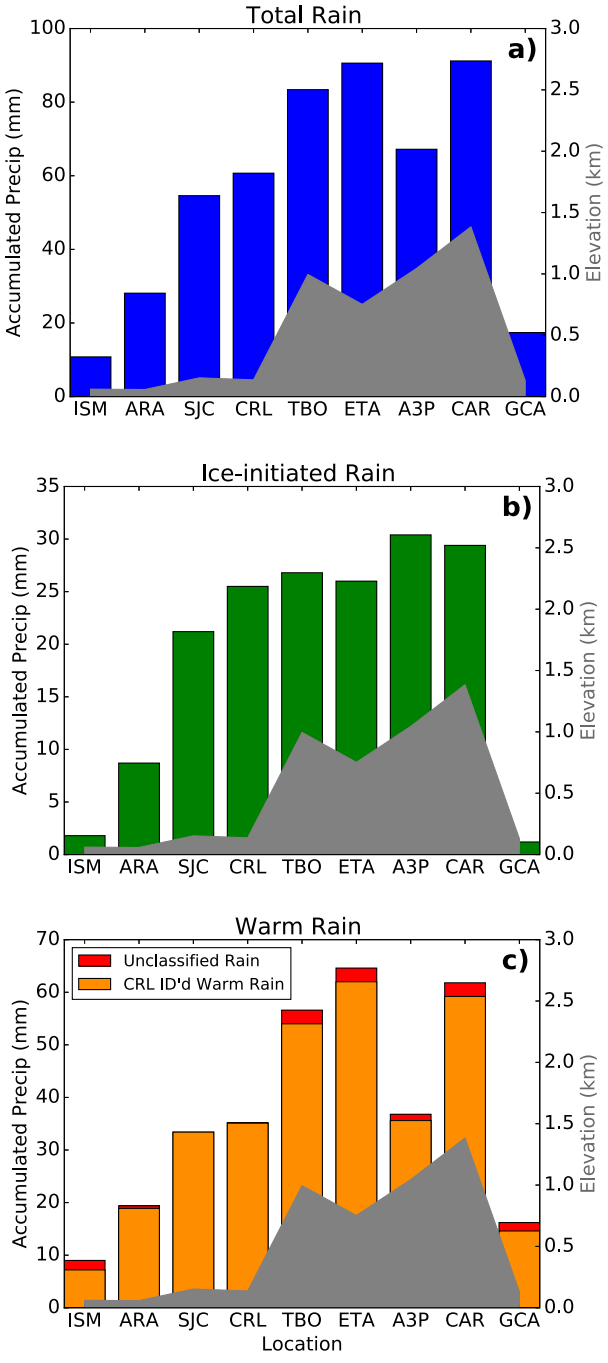

FIG. 6. Accumulated rainfall for (a) all precipitation periods, (b) objectively determined ice-initiated periods (7 h), and (c) objectively determined warm rain periods (10.5 h) of the 8 Jul 2015 case study. Site elevations are shown for reference in gray. Unclassified rain accumulation, which is defined by rain which occurred when accumulations were less than 0.2 mm in a half-hour period at CRL, is shown in red. There were no subjectively removed "convective" periods during the case study.

between the rain regimes, with the warm rain distribution shifted toward a slightly lower LWC (Fig. 7c). Warm rain generally has a moderately lower rain rate (Fig. 7d) and reflectivity (Fig. 7e). These observations are consistent with expectations. Without ice-initiated seeds from aloft, warm rain lacks the larger drops of ice-initiated rain yet is still capable of considerable precipitation accumulation.

The Parsivel's inability to measure small drops (diameter < 0.37 mm) should be considered when interpreting Fig. 7. For example, the Parsivel will underestimate LWC more for a warm rain regime with many small drops than an ice-initiated regime where much of the rainfall is provided by larger drops, which could explain the differences in Fig. 7c between warm and ice-initiated regimes. The Parsivel's exclusion of small drops is also expected to lead to bias in the other DSD-derived quantities. Measurements of reflectivity, rain rate, LWC, and N_d will be biased low, whereas D_m will be biased high, with biases enhanced during warm rain conditions. Since the relative influence of small drops decreases with increasing DSD moment, the relative magnitude of the bias will decrease with increasing moment. So, biases in LWC (third moment) will be higher than in rain rate (between third and fourth), which will be higher than in reflectivity (sixth). Observed biases of Parsivel rain rates relative to tipping-bucket gauge measurements are consistent with the above expectations. During warm rain periods with many small drops, the Parsivel observed a mean rain rate of 2.23 mm h^{-1}, while the CRL gauge recorded a substantially higher rain rate of 2.83 mm h^{-1}. In contrast, during ice-initiated periods, with a greater proportion of large drops the Parsivel recorded a mean rain rate (3.96 mm h^{-1}) similar to the gauge rate (3.93 mm h^{-1}).

Table 2 provides the mean and standard deviation of each quantity during each rainfall regime. A Wilcoxon rank-sum test (Devore 2015) was applied to the data to test if mean quantities are significantly different between rainfall regimes (two sided, $p = 0.01$). The results of this test indicate that the means of all tested quantities are significantly different between regimes.

b. *Orographic enhancement and its dependence on rain regime*

Figure 8 shows campaign-length rainfall accumulations during the total duration and ice-initiated and warm rain periods. Campaign-length accumulations are characterized by large increases (~350 mm difference) between ARA, CRL, and TBO. ETA has slightly more accumulation (~50 mm difference) than TBO, and there is a slight drop-off in accumulation (~60 mm) from ETA to CAR. GCA in the lee accumulates the least precipitation, about 120 mm less than ARA.

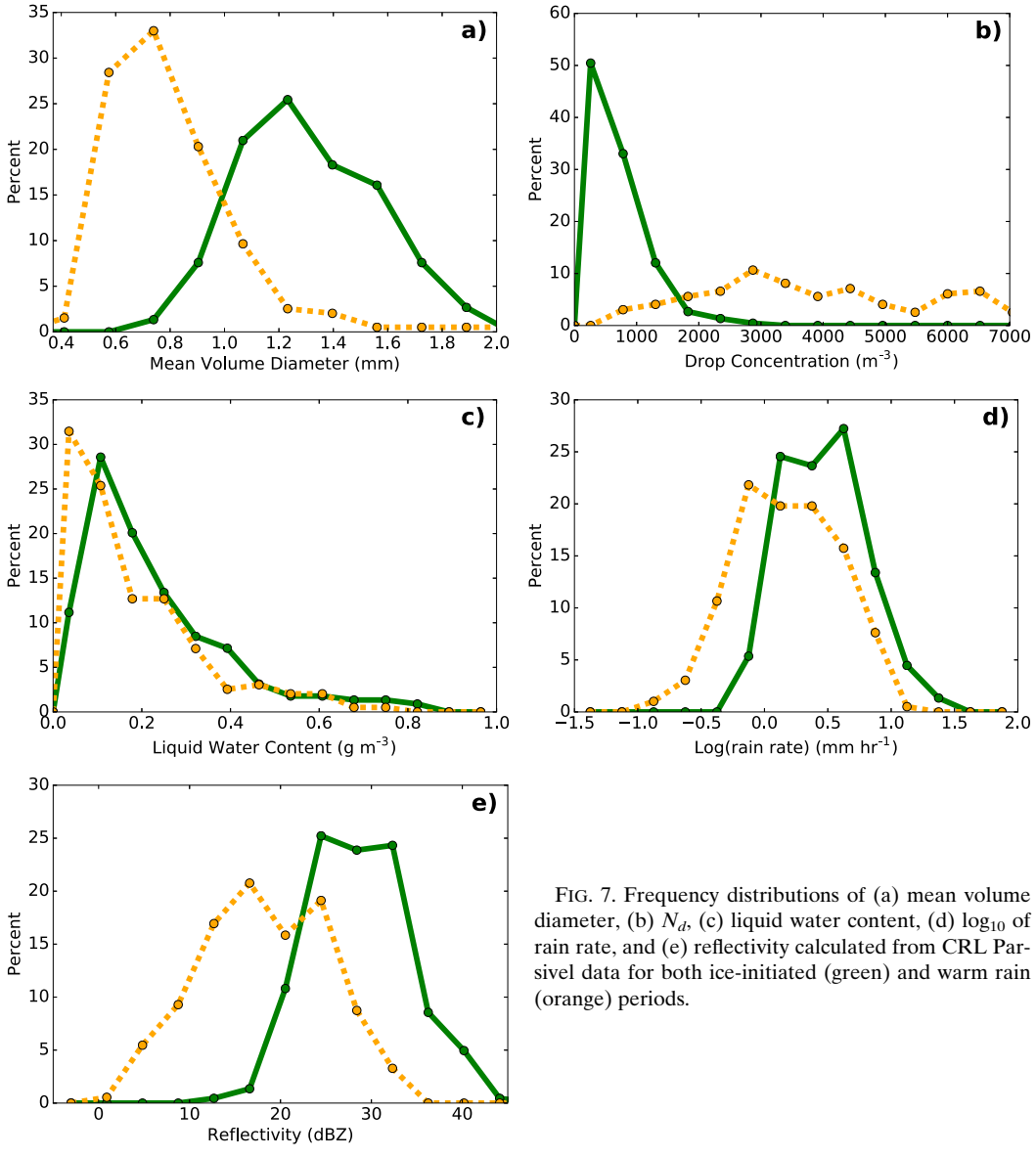

FIG. 7. Frequency distributions of (a) mean volume diameter, (b) N_d, (c) liquid water content, (d) $\log_{10}$ of rain rate, and (e) reflectivity calculated from CRL Parsivel data for both ice-initiated (green) and warm rain (orange) periods.

The duration of ice-initiated rain for which the gauge network was operational was 140 h, while the duration of warm rain was 126.5 h. During ice-initiated periods CRL accumulates roughly twice as much precipitation as ARA with a difference of about 200 mm (1.43 mm h^{-1} as a rain rate). Enhancement between the foothills and mountains is much less than between the coast and the foothills, as accumulations are relatively similar among CRL, TBO, ETA, and CAR.

During warm rain periods the enhancement between CRL and the mountain sites (~155 mm, 1.22 mm h^{-1} difference) is greater than during ice-initiated periods (~75 mm, 0.54 mm h^{-1} difference). CRL receives roughly 3 times the precipitation as ARA during warm rain periods, with a difference of about 185 mm (1.46 mm h^{-1}). Rain rate enhancement between the foothills and the coast is similar between rain regimes. As in the case study, there is an apparent increase in orographic enhancement during warm rain periods between the foothills and the mountains. Precipitation is similarly suppressed in the lee for both types of rainfall.

Figure 8 suggests that orographic enhancement during warm rain periods is greater, but the question remains if this difference is statistically significant. Since we only have one season of data we do not know how significant seasonal differences in enhancement are, as some of the difference may be caused by variations unrelated to

TABLE 2. Mean and standard deviation of DSD-derived quantities (with the exception of "gauge rain rate," which is from the CRL rain gauge) calculated for half-hour samples of ice-initiated and warm rain. Additionally, the results of a Wilcoxon rank-sum test on a null hypothesis that there is no difference between the mean warm and ice-initiated quantities (two sided, $p = 0.01$) is provided for each quantity.

	Ice initiated ($n = 224$)		Warm rain ($n = 197$)		Wilcoxon rank-sum test	
	Mean	Std dev	Mean	Std dev	Z test statistic	p 0.01 significant?
D_m (mm)	1.30	0.25	0.80	0.27	15.2	Yes
LWC (g m^{-3})	0.23	0.18	0.17	0.15	4.5	Yes
Log_{10} (rain rate) (mm h^{-1})	0.47	0.32	0.16	0.40	7.5	Yes
Reflectivity (dBZ)	28.5	5.5	18.1	6.9	13.0	Yes
N_d (m^{-3})	638	471	5704	3697	−17.2	Yes
Rain rate (mm h^{-1})	3.96	3.54	2.23	2.20	7.5	Yes
Gauge rain rate (mm h^{-1})	3.93	2.94	2.83	2.23	4.6	Yes

rainfall regime. One way to test the robustness of these differences is to break the data into smaller samples such that differences between regimes can be compared to variability and statistical significance can be ascertained. Three primary components of such an orographic enhancement significance framework that must be identified and justified: 1) choice of metric, 2) sampling window over which to calculate metric, and 3) how to incorporate gauge data into metric.

SIGNIFICANCE OF REGIME-DEPENDENT OROGRAPHIC ENHANCEMENT

To quantify orographic enhancement, we use the orographic difference, defined as $R_{\text{mtn}} - R_{\text{up}}$, where R_{mtn} is mountain precipitation accumulation (e.g., TBO, ETA, CAR) and R_{up} is upwind precipitation accumulation (e.g., ARA). The primary justification for this choice is that orographic difference quantifies the absolute amount of precipitation increase in the mountains relative to background or upwind values, and unlike the orographic ratio ($R_{\text{mtn}}/R_{\text{up}}$) is invariant to changes to domainwide precipitation.

We calculate the orographic difference over sampling periods of 2 and 3 h, during which rain classification must be homogeneous throughout the sampling period. A 2-h sampling period yields more samples, while a 3-h sampling period yields fewer samples but targets sustained periods of consistent rain regime.

All available gauge data from the campaign-length time series are used, with the exception of GCA since it is not relevant for windward enhancement. This leaves ARA, CRL, TBO, ETA, and CAR. However, there is still uncertainty as to which rain gauge or average of rain gauges from the network should be used for R_{mtn} and R_{up}. One potential source of systematic error that should be considered is gauge undercatch. The smaller drop size distributions of warm rain may cause more exposed gauge locations to experience greater undercatch during warm rain periods than during ice-initiated periods. If an exposed gauge is included in an estimate of R_{mtn}, the statistical test would be biased away from considering warm rain orographic enhancement greater. Conversely, if an exposed gauge is included in an estimate of R_{up}, the statistical test would be biased toward considering warm rain orographic enhancement greater.

Our approach to overcoming the above-described systematic and methodological uncertainties is to calculate a suite of many different orographic enhancement metrics in which the time step, R_{up}, and R_{mtn} are varied. The significance of differences between warm and ice-initiated samples is then tested for each different metric. Figure 9 provides a schematic summary of all the different orographic enhancement metrics calculated. The statistical test is run for the orographic difference calculated using a 2-h time step and a 3-h time step, for each of 1) ARA as R_{up}, 2) CRL as R_{up}, and 3) CRL and ARA averaged together for R_{up}. While ARA is the best location to estimate upwind precipitation, CRL is also used so that any systematic biases in the ARA precipitation time series do not have a disproportionate impact on results. For each of these six combinations, every possible combination of lone mountain sites and groups of mountain sites averaged together is used for R_{mtn}. In the case where ARA is R_{up}, CRL is considered a mountain site. Conversely, if CRL is included in R_{up}, it is not included in R_{mtn} combinations. This yields 58 different configurations for the statistical test.

A Wilcoxon rank-sum test (Devore 2015) is used to test if mean warm rain orographic enhancement is significantly different from ice-initiated rain for each of the 58 different test configurations ($p = 0.05$, two sided). For tests with a 2-h (3-h) time step, there are 37 (18) samples of warm rain orographic enhancement and 43 (23) samples of ice-initiated orographic enhancement. Not

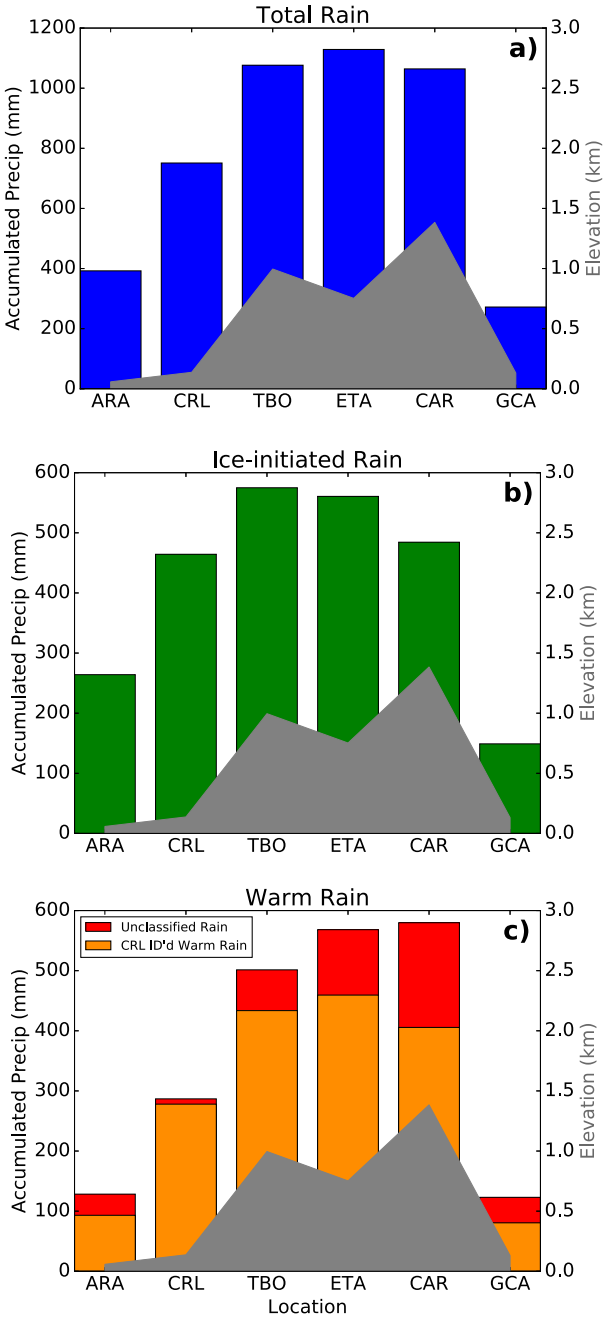

FIG. 8. Campaign-length rain gauge accumulations for (a) all nonconvective precipitation periods, (b) ice-initiated periods (140 h), and (c) warm rain periods (126.5 h). For reference, elevations are shown in gray. Unclassified rain is rain that fell during half hour periods when less than 0.2 mm fell at CRL.

all of these samples are completely independent. For example, 2-h (3-h) sampling yields 18 (8) warm rain and 12 (3) ice-initiated samples that are temporally consecutive to other samples of the same regime and which may be partially autocorrelated. However, conservative removal of these consecutive samples would leave a sample size large enough (n, $m > 8$) to assume that the test statistic is normally distributed. Therefore, a traditional p value can be calculated (Devore 2015).

Figure 10 presents the distribution of p values calculated by applying the Wilcoxon rank-sum test to each of the 58 configurations. For about 38% of the configurations, warm rain enhancement is significantly greater than ice-initiated orographic enhancement. Additionally, the location of each configuration on the normal distribution of the test statistic is shown. None of the tests suggest that enhancement is greater during ice-initiated rain periods. Additionally, TBO is the most exposed rain gauge used in the analysis, leading to concern that increases in undercatch during warm rain periods would cause an underestimation of warm rain enhancement relative to ice-initiated enhancement for metrics that include TBO. The partitioning in Fig. 10 shows a substantial shift in the distribution toward a significant result if the TBO gauge is excluded from the analysis. This demonstration highlights the nonnegligible uncertainty involved when using observations from a relatively sparse gauge network and short sample size.

We conclude that while there is a suggestion that warm rain enhancement is greater, the statistical significance of the difference is ambiguous because of methodological uncertainties. In the future, rain gauge observational uncertainty could be constrained by using more sophisticated collection systems such as pit rain gauges, constructing more sheltered site locations or placing wind shielding around gauges, and colocating multiple rain gauges at individual locations (Sieck et al. 2007). Even with observational uncertainty, CCOPE precipitation data suggest that seeding from ice aloft is not a requirement for large amounts of orographic enhancement.

c. *Radiosonde-derived quantities and orographic enhancement*

In addition to microphysical differences between the regimes, one cannot rule out dynamical differences between the regimes as a cause of differences in orographic precipitation patterns. For example, stronger orographic enhancement could be caused by stronger moisture flux (high IWV flux), and weaker orographic enhancement could be caused by increased blocking (high $N_m H/U$).

Of the 26 sounding launches, 9 were launched during warm rain periods and 10 were launched during ice-initiated periods. Table 3 presents mean quantities from sounding launches for a 500–2000-m layer of the atmosphere. Mean values are fairly similar for each metric

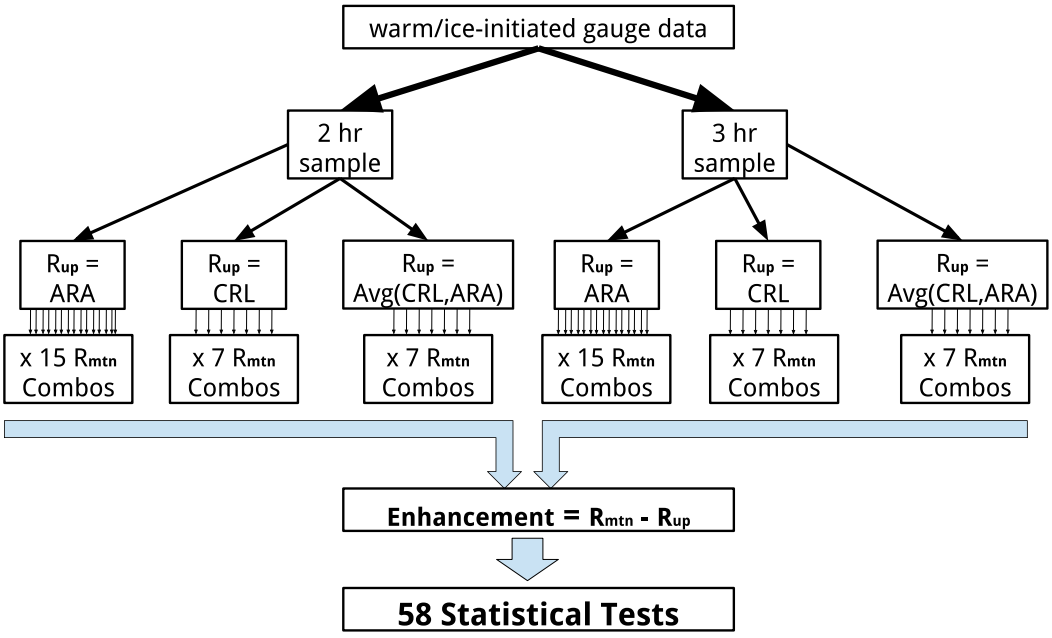

FIG. 9. Diagram of all of the methods used for calculating orographic difference.

and none of the differences in sounding parameters between regimes are significant. IWV flux and wind speed are greater during ice-initiated periods, but this would be consistent with increased enhancement during ice-initiated rain. Thus, these data, although limited, do not offer support for systematic differences in dynamics or moisture flux between regimes as an explanation for observed orographic precipitation patterns.

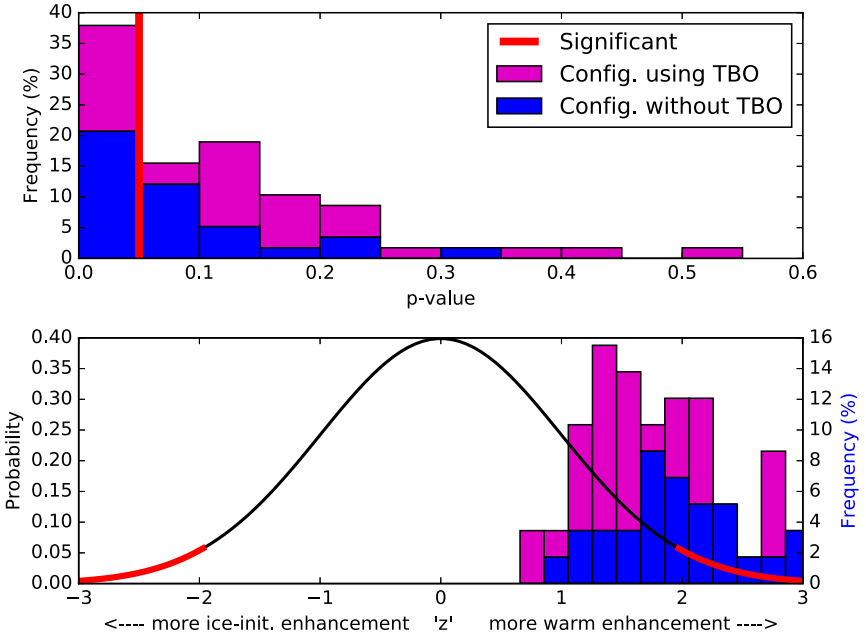

FIG. 10. (top) Distribution of p values resulting from each of the 58 statistical tests. Tests with p values less than 0.05 are considered statistically significant. (bottom) Position of test statistics from each of the 58 statistical tests on the normal distribution of the test statistics. Significance is achieved for tests with statistics greater than 1.96 or less than 1.96. Additionally, each test is color coded as to whether TBO was included in calculating R_{mn}. TBO is the most exposed site in the analysis and may experience preferentially more undercatch during warm rain regimes.

TABLE 3. Mean and standard deviation of sounding-derived quantities for ice-initiated and warm rain periods in a layer of the atmosphere between 500 and 2000 m MSL. Wind direction and moisture flux direction varied by less than a degree, so only wind direction is presented. Additionally, the results of a Wilcoxon rank-sum test on a null hypothesis that there is no difference between the mean warm and ice-initiated quantities (two sided, $p = 0.05$) is provided for each quantity.

	Ice initiated ($n = 10$)	Warm rain ($n = 9$)	Wilcoxon rank-sum test	
	Mean	Mean	Z test statistic	p 0.05 significant?
$N_m H/U$	0.61	0.62	0.41	No
N_m (s^{-1})	0.0083	0.0073	−0.41	No
IWV flux ($mm\,m^{-1}\,s^{-1}$)	206	163	−1.55	No
IWV (mm)	9.9	10.9	1.39	No
$\overline{T}$ (°C)	5.6	6.1	0.90	No
Wind speed ($m\,s^{-1}$)	20.9	15.3	−1.55	No
Wind direction (°)	334	318	−1.47	No

5. Comparison of orographic precipitation between the Nahuelbuta and the California Coast Range

We now compare CCOPE observations from the previous section to research done in the California Coast Range. The percentage of precipitation falling as warm rain in California is 28% at Bodega Bay on the coast (averaged over two seasons) and 32.2% at Cazadero in the mountains (averaged over 15 seasons; White et al. 2015), which compares closely to observations at CRL (33%). Despite differences in geography between the two locations, CRL is likely a closer analog to Cazadero than Bodega Bay. While CRL is located in the foothills and not near the top of the barrier like Cazadero, it shares very few similarities to Bodega Bay, which is located in coastal lowlands several kilometers from significant terrain.

a. Comparison of DSD-derived quantities

Figure 7 and Table 2 are analogous to Fig. 6 and Table 2 from Martner et al. (2008). Key differences are that Martner et al. (2008) uses a Joss–Waldvogel disdrometer, which more accurately detects small drops, and Martner et al.'s (2008) Fig. 6 combines data from two sites, Bodega Bay (coast) and Cazadero (mountain). A departure in our approach from Martner et al. (2008) is that we analyze average volumetric number concentration (in units of particles per unit volume), while Martner et al. (2008) analyzes the total number of drops measured by the instrument in a given period (in units of particles per unit time). Volumetric number concentration is used here since it is more readily related to other DSD quantities.

Like CCOPE, Martner et al.'s (2008) California Coast Range research found rain rate, reflectivity, D_m, and N_d to be significantly smaller during warm rain than during ice-initiated periods. One difference between CCOPE and Martner et al. (2008) is that in California there is no statistically significant difference in LWC, while in the Nahuelbuta warm rain LWC was less than ice-initiated LWC. Warm rain D_m is also greater in CRL than the California sites. However, both of these differences between California and the Nahuelbuta can potentially be explained by the previously discussed Parsivel biases associated with its effective detection threshold.

b. Comparison of orographic enhancement

Kingsmill et al. (2016) examined orographic enhancement over a much larger (10 years) sample size by calculating the orographic ratio between Bodega Bay (coast) and Cazadero (mountain) in California and found the orographic ratio to be greater during warm rain events than ice-initiated events. The use of the orographic ratio makes it difficult to assess if this difference is due to increased absolute enhancement or decreased background precipitation during warm rain periods, so we use Tables 2 and 3 from Kingsmill et al. (2016) to calculate the orographic difference from annual mean rain rates at Cazadero and Bodega Bay. The mean orographic difference for ice-initiated periods was $3.0\,mm\,h^{-1}$, while the mean orographic difference for warm rain periods was $2.5\,mm\,h^{-1}$. As observed during CCOPE, orographic enhancement is strong for both rain regimes. However, the California data suggest that ice-initiated, rather than warm rain, has greater enhancement. This difference in enhancement between rain regimes was not significant ($p = 0.05$), but for all but one year (2010/11) the orographic difference was greater during ice-initiated periods than warm rain periods. Despite the observed similarities in DSDs between the Nahuelbuta and California, the data suggest that orographic enhancement varies as a function of rain regime differently between the two study regions. This difference could be due to physical differences in geography or aerosols, but could also be a result of limited temporal sampling in the Nahuelbuta (1 year of data) and/or limited spatial sampling in California (two rain gauges).

One possible explanation is that warm rain clouds may induce more orographic enhancement in the interior of coastal mountain ranges relative to the windward slopes due to longer microphysical time scales. Any increase in enhancement in the interior of the mountains would be better represented by the CCOPE dataset because the CCOPE rain gauge network sampled the interior peaks better than the California dataset.

c. Comparison of upwind flow characteristics

Kingsmill et al. (2016) used a GPS receiver to calculate IWV, a wind profiler to observe low-level winds, and the product of the two measurements to calculate a bulk index of IWV flux in coastal California. They found IWV to be about 5% greater during warm rain periods. CCOPE soundings suggest that lower tropospheric IWV in the Nahuelbuta is also greater (~10%) during warm rain periods. Given that Kingsmill et al. (2016) estimated the total IWV in the atmosphere and warm rain periods are expected to have lower relative humidity aloft, one would expect the difference of IWV between regime to be less for his dataset than for our low-level IWV. Kingsmill et al.'s (2016) dataset could not reveal if this increased IWV during warm rain is due to increased temperature. CCOPE data found mean temperatures during warm rain soundings to be marginally greater (0.5°C), which, given the near-saturated conditions, can partially explain the increased IWV (expected ~4% increase in IWV with 0.5°C warming).

Kingsmill et al. (2016) found IWV flux and mean upslope flow to be 16% and 19% larger during warm rain periods. We see the opposite relationship in our data. One possible explanation is that we have calculated the magnitude of IWV flux and wind, while Kingsmill et al. (2016) calculated these quantities parallel to a cross-terrain vector. This is relevant because in both the Nahuelbuta and California data there is a suggestion that winds are more westerly during warm rain periods. In the Kingsmill et al. (2016) data the primary wind direction was ~170° for ice-initiated rain and ~205° for warm rain periods. For Kingsmill et al. (2016) this warm rain wind shift brings the flow more in-line with the cross-terrain vector.

6. Summary and conclusions

CCOPE used soundings, two MRR profiling radars, a Parsivel disdrometer, and a rain gauge network to characterize warm and ice-initiated rain regimes and explore their consequences for coastal orographic precipitation over Chile's Nahuelbuta Mountains from 22 May to 14 August 2015.

A case study provided detailed observations of each rain regime. In this example, ice-initiated rain was characterized by more synoptic forcing for midtropospheric ascent, upwind soundings with a deep layer of saturation and weak stability, fewer but larger raindrops, and strong orographic enhancement. Warm rain was characterized by weaker synoptic forcing for midtropospheric ascent, weak stability, a shallower upwind layer of saturated air, and many but smaller drops. Orographic enhancement was strong in both regimes. Rain rates during warm rain periods were generally of similar magnitude as ice-initiated rain rates at mountain sites, but were lighter or absent at upwind locations. Sounding launches suggest that differences in orographic enhancement are not simply explainable by differences in low-level moisture flux or orographic airflow dynamics between the regimes.

The rain gauge network observed 140 h of ice-initiated rain and 126.5 h of warm rain. Enhancement between the coast and the foothills was similar between regimes (~1.45 mm h^{-1} difference), while enhancement between the foothills and mountains was greater during warm rain periods (~1.22 mm h^{-1} difference) than ice-initiated periods (~0.54 mm h^{-1}). We tested if this difference was statistically significant, incorporating methodological uncertainty by varying how orographic enhancement is quantified. Thirty-eight percent of statistical tests found warm rain enhancement to be significantly greater (two sided, $p = 0.05$). No statistical test indicated greater ice-initiated enhancement. Removing a particularly exposed site that could preferentially underestimate rain during warm rain periods shifted the distribution of tests toward a more significant result, highlighting the importance of constraining methodological uncertainty in measurements of orographic enhancement. Despite uncertainty, our data suggest that seeding from ice aloft is not a requirement for large orographic enhancement, and may be a minor determinant, relative to low-level moisture source, of precipitation amount.

The total portion of warm rain (~33% of total), DSDs, and strong orographic enhancement in both rain regimes were found to be very similar to observations in the California Coast Range (Martner et al. 2008; Kingsmill et al. 2016). However, in the California Coast Range absolute enhancement was greater during ice-initiated periods than warm rain periods. This difference in orographic enhancement as a function of rain regime could be due to differences in spatial and temporal sampling between the two field projects. Generally, warm rain characteristics and occurrence are similar between the two study areas. These similarities hold despite possible differences in aerosol concentrations,

suggesting they may have a minor control on orographic warm rain. Both locations likely have an ample source of sea salt aerosols from the Pacific Ocean, which may help enable efficient warm rain autoconversion if giant CCN are present. Because warm rain regimes contribute substantial orographic precipitation in diverse locations, future research, including a Universidad de Chile–led CCOPE modeling project, will focus on identifying and quantifying the processes that control warm rain microphysical efficiency and how they are modulated by synoptic and mesoscale conditions.

Acknowledgments. This material is based upon work supported by National Science Foundation Grants AGS-1522277, AGS-1522939, and AGS-1144271, and Comisión Nacional de Investigación Científica y Tecnológica (Chile) Grants CHRIAM/FONDAP-15130015 and CR2/FONDAP-15110009. We acknowledge the Departamento de Geofísica at the Universidad de Concepción for hosting researchers during the campaign. Freddy Echeverría-Cabezas organized many of the campaign logistics. Yazmina Rojas-Beltran, Matias Guzman-Muñoz, Daniel Veloso-Aguila, Nicolas Garcia-Lee, and Camilo Márquez helped with sounding launches. Daniel Veloso-Aguila also aided with field work and Nicolas Garcia-Lee helped install the Isla de Santa María rain gauge. Dr. Alberto Foppiano-Bachmann piloted the aircraft to the Isla de Santa María. The manuscript also benefited substantially from the comments of two anonymous reviewers.

APPENDIX A

Evaluation of MRR versus SPROF

We deployed one of the CCOPE MRRs at NOAA's Cazadero, California, research site (White et al. 2003) from December 2014 to March 2015 to compare with NOAA's more sophisticated 3-GHz S-band profiler (SPROF). The goal was to evaluate the MRR's ability to measure vertical precipitation structures against a radar specifically designed to observe heavy rain.

Figure A1 shows a comparison of median profiles between the MRR and the SPROF for SPROF-identified ice-initiated and warm rain periods. During warm rain periods (Figs. A1a,b), the median reflectivity profiles rapidly decrease with increasing height, as observed in White et al. (2003), and are consistent with low-level growth via collision–coalescence in liquid clouds. The MRR reports consistently lower reflectivities than the SPROF, but a similar vertical gradient. During warm rain periods, the typically low reflectivity values above 2 km are not detected by the MRR because of its limited sensitivity. Unlike reflectivity values, the MRR overestimates Doppler velocity relative to the SPROF. This may also be attributed to the decreased sensitivity of the MRR relative to the SPROF. During warm rain periods the SPROF can detect lighter precipitation, which would be more likely to have lower fall speeds. This would skew the median profile toward lower values relative to the MRR, as observed. This, and the mild differences in vertical reflectivity gradients, suggests that during warm rain periods observed differences between the MRR and the SPROF are more likely to be caused by the low sensitivity of the MRR than attenuation.

During ice-initiated rain periods (Figs. A1c,d), the SPROF data have a well-defined local maxima in reflectivity at the melting level, which is not reflected in the MRR data, most likely due to severe attenuation at the brightband. Reflectivities above the brightband are much less in the MRR profile than the SPROF profile. The MRR overestimates Doppler velocity at and below the melting level by up to $\sim 1\,\mathrm{m\,s^{-1}}$. The median Doppler vertical velocity profile below the melting level exceeds the Nyquist range ($\pm 6\,\mathrm{m\,s^{-1}}$) of the instrument, so the Doppler velocity at these levels depends on the dealiasing routine used by Maahn and Kollias (2012). It appears that attenuation and uncertainty due to Maahn and Kollias postprocessing is larger during ice-initiated periods than warm rain periods. This was expected, as both sources of error increase with increasing drop size, and ice-initiated rain usually has larger drops (Martner et al. 2008).

Given the discrepancies between the SPROF and MRR profiles, MRR profiles are mostly used in a qualitative manner in this study. The only exception is that MRR Doppler velocity data are used to identify and quantify the melting level as described in appendix B.

APPENDIX B

Development of MRR-Based Ice-Initiated Detection Algorithm

The phase change of falling precipitation from ice to water manifests itself in profiling radar observations in two ways: 1) it causes a local maxima in reflectivity due to large, partially melted ice and snow and 2) it causes fall (Doppler[1]) velocity to increase as precipitation melts, resulting in an increase in fall velocity with decreasing altitude. White et al. (2003) used these two principles to develop an objective algorithm for

[1] We have picked positive Doppler velocity to be toward the radar.

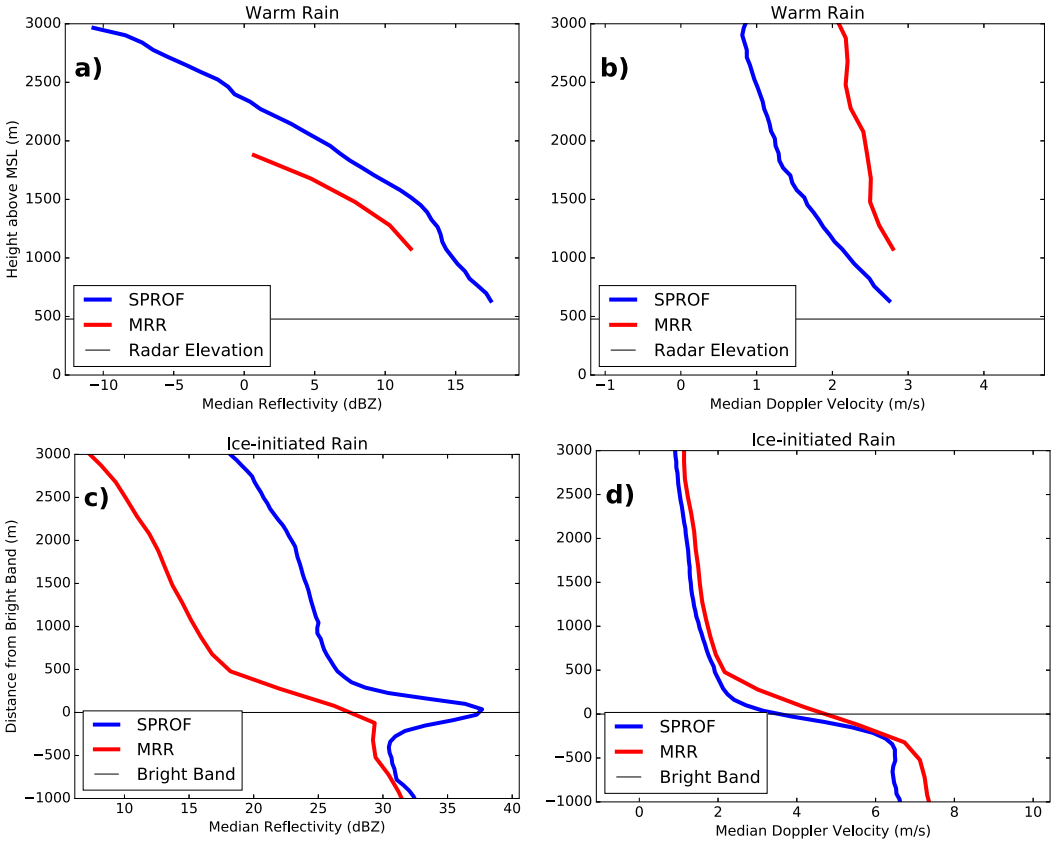

FIG. A1. Median profiles during warm rain for (a) reflectivity and (b) Doppler velocity. Additionally, median profiles during ice-initiated rain of (c) reflectivity and (d) Doppler velocity. Note there is a change in *x*-axis scale between warm and ice-initiated plots. Data are from the MRR–SPROF comparison from December 2014 to March 2015 in Cazadero. Median reflectivity profiles are the median of the total sample size, assuming that undetectable reflectivities for each instrument are some reflectivity below the detection limit. Median Doppler velocity profiles are the median of the detectable samples at each level. Note that the elevation of profiles during ice-initiated periods (c) and (d) are relative to the SPROF-determined brightband elevation.

brightband detection using SPROF profiling radar data. In their algorithm, for each half-hour period in which a site experiences greater than 0.5 mm of rain accumulation, a designation of brightband is applied if 50% or greater of the SPROF profiles during the period have collocated gradients in reflectivity greater than 2.5 dBZ_e per 210 m (associated with a maxima in reflectivity) and gradients in Doppler vertical velocity less than $-1.5\,\mathrm{m\,s^{-1}}$ per 210 m.

Similar principles were used to develop an MRR detection algorithm for ice-initiated rain. However, because attenuation due to the K-band wavelength obscures the local maxima in reflectivity (appendix A), we use gradients in Doppler velocity alone. Our algorithm uses two parameters: 1) the threshold of Doppler velocity gradient associated with melting and 2) the percentage of profiles in a half-hour sample that must exhibit this Doppler velocity gradient for that period to be classified as ice-initiated. The combination of these two tunable parameters that minimizes the error between MRR ice-initiated rain detection and SPROF ice-initiated detection during the Cazadero comparison is used for CCOPE ice-initiated detection. Error is defined as the total number of half-hour periods in which the MRR either falsely detects a melting layer or fails to detect a melting layer.

The optimized MRR parameters are $-1.16\,\mathrm{m\,s^{-1}}$ per 210 m and 35% of profiles in a half-hour sample required to identify a melting layer. Using these parameters, as compared to the SPROF, the MRR ice-initiated detection algorithm has a probability of detection of 0.99 and a false alarm ratio of 0.08 for the duration of the Cazadero deployment. The melting layer height bias was −12.5 m, and the root-mean-square error (RMSE) of the height was 108 m, which is strong performance given that the configured range resolution of the MRR was only 200 m (compared with 60 m for the SPROF). Ideally, one would develop the MRR algorithm on a

subset of the data and test the performance on a different portion. However, the short duration of the comparison campaign in Cazadero did not allow for a sample size large enough to employ this procedure. Despite this weakness, the performance of the algorithm provides confidence that the MRR is able to correctly detect the melting layer.

REFERENCES

Adirosi, E., L. Baldini, N. Roberto, P. Gatlin, and A. Tokay, 2016: Improvement of vertical profiles of raindrop size distribution from micro rain radar using 2D video disdrometer measurements. *Atmos. Res.*, **169**, 404–415, doi:10.1016/j.atmosres.2015.07.002.

Bader, M., and W. Roach, 1977: Orographic rainfall in warm sectors of depressions. *Quart. J. Roy. Meteor. Soc.*, **103**, 269–280, doi:10.1002/qj.49710343605.

Baines, P. G., and R. B. Smith, 1993: Upstream stagnation points in stratified flow past obstacles. *Dyn. Atmos. Oceans*, **18**, 105–113, doi:10.1016/0377-0265(93)90005-R.

Bennartz, R., 2007: Global assessment of marine boundary layer cloud droplet number concentration from satellite. *J. Geophys. Res.*, **112**, D02201, doi:10.1029/2006JD007547.

Bergeron, T., 1949: The problem of artificial control of rainfall on the globe: II. The coastal orographic maximum of precipitation in autumn and winter. *Tellus*, **1**, 15–32, doi:10.1111/j.2153-3490.1949.tb01264.x.

——, 1965: On the low-level redistribution of atmospheric water caused by orography. *Proc. Int. Conf. on Cloud Physics*, Tokyo, Japan, Japan. Meteorological Agency, 96–100.

Blanchard, D. C., 1953: Raindrop size-distribution in Hawaiian rains. *J. Meteor.*, **10**, 457–473, doi:10.1175/1520-0469(1953)010<0457:RSDIHR>2.0.CO;2.

Browning, K. A., F. F. Hill, and C. W. Pardoe, 1974: Structure and mechanism of precipitation and effect of orography in a wintertime warm sector. *Quart. J. Roy. Meteor. Soc.*, **100**, 309–330, doi:10.1002/qj.49710042505.

Cannon, D. J., D. J. Kirshbaum, and S. L. Gray, 2012: Under what conditions does embedded convection enhance orographic precipitation? *Quart. J. Roy. Meteor. Soc.*, **138**, 391–406, doi:10.1002/qj.926.

Carruthers, D. J., and T. W. Choularton, 1983: A model of the feeder–seeder mechanism of orographic rain including stratification and wind-drift effects. *Quart. J. Roy. Meteor. Soc.*, **109**, 575–588, doi:10.1002/qj.49710946109.

Coplen, T. B., P. J. Neiman, A. B. White, and F. M. Ralph, 2015: Categorisation of northern California rainfall for periods with and without a radar brightband using stable isotopes and a novel automated precipitation collector. *Tellus*, **67B**, 28574, doi:10.3402/tellusb.v67.28574.

Devore, J., 2015: *Probability and Statistics for Engineering and the Sciences.* Cengage Learning, 768 pp.

Douglas, C., and J. Glasspoole, 1947: Meteorological conditions in heavy orographic rainfall in the British Isles. *Quart. J. Roy. Meteor. Soc.*, **73**, 11–42, doi:10.1002/qj.49707331503.

Durran, D. R., and J. B. Klemp, 1982: On the effects of moisture on the Brunt–Väisälä frequency. *J. Atmos. Sci.*, **39**, 2152–2158, doi:10.1175/1520-0469(1982)039<2152:OTEOMO>2.0.CO;2.

Fabry, F., 2015: *Radar Meteorology: Principles and Practice.* Cambridge University Press, 272 pp.

Falvey, M., and R. Garreaud, 2007: Wintertime precipitation episodes in central Chile: Associated meteorological conditions and orographic influences. *J. Hydrometeor.*, **8**, 171–193, doi:10.1175/JHM562.1.

Fontannaz, C., 2001: Estadistica Climatologia Tomo II. Tech. Rep., Direccion Meteorologica de Chile, 516 pp. [Available online at http://164.77.222.61/climatologia/publicaciones/Estadistica_ClimatologicaII.pdf.]

Garreaud, R., 2013: Warm winter storms in central Chile. *J. Hydrometeor.*, **14**, 1515–1534, doi:10.1175/JHM-D-12-0135.1.

——, M. Falvey, and A. Montecinos, 2016: Orographic precipitation in coastal southern Chile: Mean distribution, temporal variability, and linear contribution. *J. Hydrometeor.*, **17**, 1185–1202, doi:10.1175/JHM-D-15-0170.1.

Hamilton, D. S., L. A. Lee, K. J. Pringle, C. L. Reddington, D. V. Spracklen, and K. S. Carslaw, 2014: Occurrence of pristine aerosol environments on a polluted planet. *Proc. Natl. Acad. Sci. USA*, **111**, 18 466–18 471, doi:10.1073/pnas.1415440111.

Hill, F. F., K. A. Browning, and M. J. Bader, 1981: Radar and rain-gauge observations of orographic rain over south Wales. *Quart. J. Roy. Meteor. Soc.*, **107**, 643–670, doi:10.1002/qj.49710745312.

Hobbs, P. V., 1978: Organization and structure of clouds and precipitation on the mesoscale and microscale in cyclonic storms. *Rev. Geophys.*, **16**, 741–755, doi:10.1029/RG016i004p00741.

Houze, R. A., Jr., and Coauthors, 2017: The Olympic Mountains Experiment (OLYMPEX). *Bull. Amer. Meteor. Soc*, doi:10.1175/BAMS-D-16-0182.1, in press.

Hughes, M., A. Hall, and R. Fovell, 2009: Blocking in areas of complex topography, and its influence on rainfall distribution. *J. Atmos. Sci.*, **66**, 508–518, doi:10.1175/2008JAS2689.1.

Jensen, J. B., and A. D. Nugent, 2017: Condensational growth of drops formed on giant sea-salt aerosol particles. *J. Atmos. Sci.*, **74**, 679–697, doi:10.1175/JAS-D-15-0370.1.

Jiang, Q. F., and R. B. Smith, 2003: Cloud timescales and orographic precipitation. *J. Atmos. Sci.*, **60**, 1543–1559, doi:10.1175/2995.1.

Johnson, D. B., 1982: The role of giant and ultragiant aerosol particles in warm rain initiation. *J. Atmos. Sci.*, **39**, 448–460, doi:10.1175/1520-0469(1982)039<0448:TROGAU>2.0.CO;2.

Joss, J., and A. Waldvogel, 1967: Ein spektrograph für niederschlagstropfen mit automatischer auswertung. *Pure Appl. Geophys.*, **68**, 240–246, doi:10.1007/BF00874898.

Kingsmill, D. E., P. J. Neiman, and A. B. White, 2016: Microphysics regime impacts on the relationship between orographic rain and orographic forcing in the coastal mountains of Northern California. *J. Hydrometeor.*, **17**, 2905–2922, doi:10.1175/JHM-D-16-0103.1.

Maahn, M., and P. Kollias, 2012: Improved Micro Rain Radar snow measurements using Doppler spectra post-processing. *Atmos. Meas. Tech.*, **5**, 2661–2673, doi:10.5194/amt-5-2661-2012.

Martner, B. E., S. E. Yuter, A. B. White, S. Y. Matrosov, D. E. Kingsmill, and F. M. Ralph, 2008: Raindrop size distributions and rain characteristics in California coastal rainfall for periods with and without a radar bright band. *J. Hydrometeor.*, **9**, 408–425, doi:10.1175/2007JHM924.1.

Miltenberger, A. K., A. Seifert, H. Joos, and H. Wernli, 2015: A scaling relation for warm-phase orographic precipitation: A Lagrangian analysis for 2D mountains. *Quart. J. Roy. Meteor. Soc.*, **141**, 2185–2198, doi:10.1002/qj.2514.

Minder, J., D. Durran, G. Roe, and A. Anders, 2008: The climatology of small-scale orographic precipitation over the Olympic Mountains: Patterns and processes. *Quart. J. Roy. Meteor. Soc.*, **134**, 817–839, doi:10.1002/qj.258.

Neiman, P. J., F. M. Ralph, A. B. White, D. E. Kingsmill, and P. O. G. Persson, 2002: The statistical relationship between upslope flow and rainfall in California's coastal mountains: Observations during CALJET. *Mon. Wea. Rev.*, **130**, 1468–1492, doi:10.1175/1520-0493(2002)130<1468:TSRBUF>2.0.CO;2.

——, G. A. Wick, F. M. Ralph, B. E. Martner, A. B. White, and D. E. Kingsmill, 2005: Wintertime nonbrightband rain in California and Oregon during CALJET and PACJET: Geographic, interannual, and synoptic variability. *Mon. Wea. Rev.*, **133**, 1199–1223, doi:10.1175/MWR2919.1.

——, B. J. Moore, A. B. White, G. A. Wick, J. Aikins, D. L. Jackson, J. R. Spackman, and F. M. Ralph, 2016: An airborne and ground-based study of a long-lived and intense atmospheric river with mesoscale frontal waves impacting California during CalWater-2014. *Mon. Wea. Rev.*, **144**, 1115–1144, doi:10.1175/MWR-D-15-0319.1.

Nešpor, V., and B. Sevruk, 1999: Estimation of wind-induced error of rainfall gauge measurements using a numerical simulation. *J. Atmos. Oceanic Technol.*, **16**, 450–464, doi:10.1175/1520-0426(1999)016<0450:EOWIEO>2.0.CO;2.

OTT, 2009: Operating instructions: Present Weather Sensor Parsivel. OTT, 48 pp. [Available online at https://www.esrl.noaa.gov/psd/data/obs/instruments/OpticalDisdrometer.pdf.]

Peel, M. C., B. L. Finlayson, and T. A. McMahon, 2007: Updated world map of the Köppen-Geiger climate classification. *Hydrol. Earth Syst. Sci.*, **11**, 1633–1644, doi:10.5194/hess-11-1633-2007.

Peters, G., B. Fischer, H. Münster, M. Clemens, and A. Wagner, 2005: Profiles of raindrop size distributions as retrieved by microrain radars. *J. Appl. Meteor.*, **44**, 1930–1949, doi:10.1175/JAM2316.1.

Ralph, F. M., P. J. Neiman, G. A. Wick, S. I. Gutman, M. D. Dettinger, D. R. Cayan, and A. B. White, 2006: Flooding on California's Russian River: Role of atmospheric rivers. *Geophys. Res. Lett.*, **33**, L13801, doi:10.1029/2006GL026689.

Reuder, J., G. Fagerlid, I. Barstad, and A. Sandvik, 2007: Stord orographic precipitation experiment (STOPEX): An overview of phase I. *Adv. Geosci.*, **10**, 17–23, doi:10.5194/adgeo-10-17-2007.

Sieck, L. C., S. J. Burges, and M. Steiner, 2007: Challenges in obtaining reliable measurements of point rainfall. *Water Resour. Res.*, **43**, W01420, doi:10.1029/2005WR004519.

Smith, R. B., 1980: Linear theory of stratified hydrostatic flow past an isolated mountain. *Tellus*, **32**, 348–364, doi:10.3402/tellusa.v32i4.10590.

——, and I. Barstad, 2004: A linear theory of orographic precipitation. *J. Atmos. Sci.*, **61**, 1377–1391, doi:10.1175/1520-0469(2004)061<1377:ALTOOP>2.0.CO;2.

——, and Coauthors, 2012: Orographic precipitation in the tropics: The Dominica Experiment. *Bull. Amer. Meteor. Soc.*, **93**, 1567–1579, doi:10.1175/BAMS-D-11-00194.1.

Szumowski, M. J., R. M. Rauber, and H. T. Ochs III, 1999: The microphysical structure and evolution of Hawaiian rainband clouds. Part III: A test of the ultragiant nuclei hypothesis. *J. Atmos. Sci.*, **56**, 1980–2003, doi:10.1175/1520-0469(1999)056<1980:TMSAEO>2.0.CO;2.

Valenzuela, R. A., and D. E. Kingsmill, 2015: Orographic precipitation forcing along the coast of Northern California during a landfalling winter storm. *Mon. Wea. Rev.*, **143**, 3570–3590, doi:10.1175/MWR-D-14-00365.1.

Viale, M., and M. N. Nuñez, 2011: Climatology of winter orographic precipitation over the subtropical central Andes and associated synoptic and regional characteristics. *J. Hydrometeor.*, **12**, 481–507, doi:10.1175/2010JHM1284.1.

White, A. B., P. J. Neiman, F. Ralph, D. Kingsmill, and P. Persson, 2003: Coastal orographic rainfall processes observed by radar during the California land-falling jets experiment. *J. Hydrometeor.*, **4**, 264–282, doi:10.1175/1525-7541(2003)4<264:CORPOB>2.0.CO;2.

——, ——, J. M. Creamean, T. Coleman, F. M. Ralph, and K. A. Prather, 2015: The impacts of California's San Francisco Bay Area gap on precipitation observed in the Sierra Nevada during HMT and CalWater. *J. Hydrometeor.*, **16**, 1048–1069, doi:10.1175/JHM-D-14-0160.1.

Yuter, S. E., D. E. Kingsmill, L. B. Nance, and M. Loffler-Mang, 2006: Observations of precipitation size and fall speed characteristics within coexisting rain and wet snow. *J. Appl. Meteor. Climatol.*, **45**, 1450–1464, doi:10.1175/JAM2406.1.

Zagrodnik, J. P., L. A. McMurdie, and R. A. Houze Jr., 2016: Synoptic and orographic control of observed drop size distribution regimes during the OLYMPEX field campaign. *17th Conf. on Mountain Meteorology*, Burlington, VT, Amer. Meteor. Soc., 5.6. [Available online at https://ams.confex.com/ams/17Mountain/webprogram/Paper296584.html.]

Zhu, Y., and R. E. Newell, 1998: A proposed algorithm for moisture fluxes from atmospheric rivers. *Mon. Wea. Rev.*, **126**, 725–735, doi:10.1175/1520-0493(1998)126<0725:APAFMF>2.0.CO;2.